Slurry extrusion on Ceres from a convective mud-bearing mantle

Ottaviano Ruesch[1,*], Antonio Genova[2], Wladimir Neumann[3,4], Lynnae C. Quick[5], Julie C. Castillo-Rogez[6], Carol A. Raymond[6], Christopher T. Russell[7], Maria T. Zuber[2]

1: European Space Agency, European Space and Technology Center, Keplerlaan 1, 2201 AZ Noordwijk, The Netherlands; 2: Department of Earth, Atmospheric and Planetary Sciences, Massachusetts Institute of Technology, Cambridge, MA, 02139, USA; 3: Institut für Planetologie, University of Münster, 48149 Münster, Germany; 4: Institut für Planetenforschung, Deutsches Zentrum für Luft- und Raumfahrt, 12489 Berlin, Germany; 5: Center for Earth and Planetary Studies, National Air and Space Museum, Smithsonian Institution, Washington, DC 20560, USA; 6: Jet Propulsion Laboratory, California Institute of Technology, Pasadena, CA, 90019, USA; 7: Department of Earth, Planetary and Space Sciences, University of California, Los Angeles, CA, 90095, USA.

*: to whom correspondence should be addressed. Email: ottaviano.ruesch@esa.int

Ceres is a 940-km-diameter dwarf planet with a bulk composition dominated by silicates and water ice. In Ceres' partially differentiated interior, extrusive processes have led to the emplacement of kilometres high domes. Here we report the analysis of an isostatic gravity anomaly detected by the Dawn spacecraft data in association with the geologically recent dome Ahuna Mons. By modelling the isostatic anomaly with a mass concentration method, we determined that the subsurface structure includes a regional mantle uplift, which we interpret as a plume. This structure is the probable source of fluids forming Ahuna Mons and, together with the constraints from the dome's morphology, indicate a rheological regime corresponding to a mixture of brine and solid particles. This property explains the viscous relaxation and the mineralogy of the dome. The presence of a plume and of slurry material indicate recent convection in a mud-bearing mantle. The inferred slurry extrusion on Ceres differs from the water-dominated cryovolcanism of icy satellites and reveals a compositional and rheological diversity of extrusive phenomena on planetary surfaces.

Ceres is the largest body in the asteroid belt with a bulk density of 2162 kg m^{-3} [1]. It is a water ice rich protoplanet that experienced aqueous alteration in its past[2]. Between 2015-2018, the Dawn spacecraft performed a reconnaissance orbital mission of the dwarf planet. One of the primary mission goals was to characterize the extent of Ceres' internal differentiation by determining its surface and interior properties[2]. The clear identification of a centrally condensed mass implies partial differentiation of the dwarf planet[3-6]. Global scale topography analysis suggested that the upper part of the mantle, below an ~40-km thick crust, has a relatively low viscosity, consistent with liquid pore fluids[7], while leaving unanswered the nature and dynamics of the mantle, as well as its potential the link to its surface expression.

Stereo imaging[8] with Dawn's Framing Camera enabled the reconstruction of the global shape, revealing a prominent topographic dome (~4 km high and 17 km wide), named Ahuna Mons[9]. The morphology and morphometry of the dome indicate an extrusive formation mechanism involving fluid-bearing (volcanic) material, and thus an unambiguously endogenic process[9]. This origin is supported by its composition rich in sodium carbonate, the solid residue of a brine[10]. The construction of the dome is consequently related to the properties of the subsurface and, ultimately, to the extent of differentiation of Ceres. To study the interior structure of the dwarf planet, Dawn performed a gravity science investigation over a year and half of X-band radio tracking data and surface optical landmarks from the Dawn spacecraft[4]. The gravity field is represented in spherical harmonic coefficients to degree and order 18 (CERES18C) with an accuracy of ~10 mGal at the equator[4]. The low gravity to topography admittance[3-5], corroborated by rheological constraints from finite element geodynamical simulations[7], indicates that Ceres' subsurface is consistent with Airy isostatic compensation, in which large-scale topographic relief is supported by variations at the crust-mantle boundary. Under this assumption, the interior structure that best satisfies the observational geodetic constraints with a two-layer (crust and mantle) model is characterized by a crustal density ρ_{crust} = 1287 kg m^{-3}, a mean crustal thickness of 41 km, and a mantle density ρ_{mantle} =2434 kg m^{-3} (see methods)[4,5]. To characterise the subsurface beneath Ahuna Mons we perform a gravity analysis using this two-layer structure.

A novel approach to analyze gravity isostatic anomalies

After subtracting the gravity contribution of the topographic load and the isostatic compensation at the crust-mantle boundary from CERES18C gravity field (see methods), a ~50-60 mGal strong positive isostatic anomaly remains, associated with Ahuna Mons and its surroundings (Figure 1), as previously noticed[5,11].

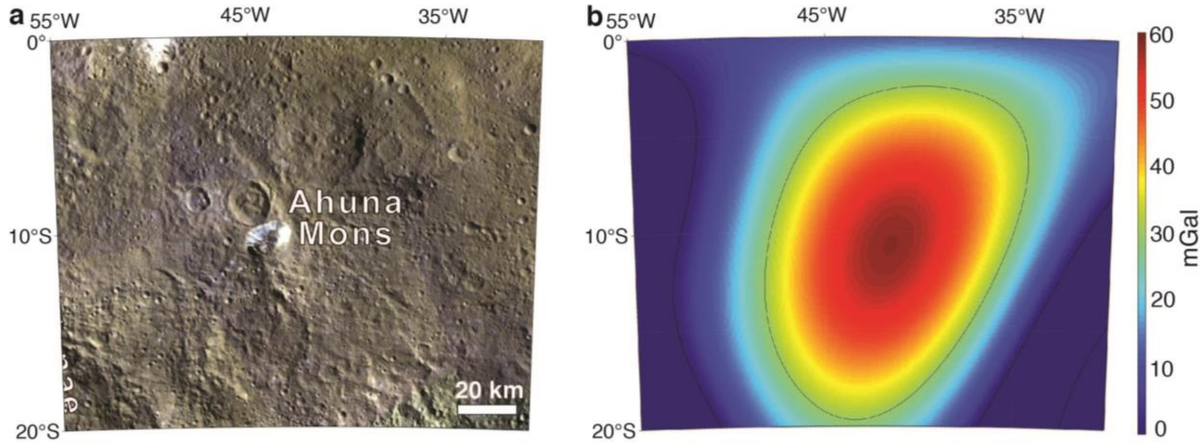

Figure 1. Co-location of volcanic dome and isostatic gravity anomaly. a, False-color mosaic (R=0.97 µm, G=0.75 µm, B=0.44 µm) of the region of Ahuna Mons from Dawn Framing Camera observations. The dome of Ahuna Mons is close to the center of the mosaic, and its high reflectance areas are steep flanks rich in carbonates and phyllosilicates[10]. **b**, Isostatic anomaly represented with spherical harmonic degrees l=5-14 and showing ~50-60 mGal at approximately the same coordinates of Ahuna Mons. Same area of panel a.

To characterize the origin of the mass concentration (mascon) that is responsible for the positive isostatic anomaly, we used a Markov-chain Monte Carlo (MCMC) technique that selects the properties of a three-dimensional ellipsoidal mass concentration (mascon), which yields gravity anomalies consistent with the measurements. The adjusted mascon parameters are density ($\Delta\rho=\rho_{mascon}-\rho_{crust}$), principal axes a, b, and c and depth (h) below the dome, as well as its geographic location and orientation (see methods). The parameters are determined non-uniquely by minimizing the anomaly between the modelled mascon gravity and the gravity derived by Dawn. The task is performed by exploiting the two-dimensional gravity anomaly map in the region of interest and not solely one-dimensional profiles. Interior model solutions that result from gravity anomaly analysis are intrinsically non-unique and, as a consequence, our method is applied with the following conditions: the mascon is assumed to be within the crust and with a density lower than the mantle density. This first condition is set by the requirements of the canonical isostatic correction because isostatic anomalies reflect density variations solely in the crust. The second assumption derives from the physical instability of a mascon with density higher than the mantle[12] and from Ceres' geophysical limitations to produce a concentration of high-density mineral species away from the body's center of mass[4,13].

A mantle uplift beneath Ahuna Mons

The results of our investigation match the observed anomaly with an uncertainty of ~6 mGal, which is fully consistent with the formal errors of CERES18C in that region of the dwarf planet (Figure 2). Two distinctive mascon configurations emerge from the final ensemble of solutions (Figure 3) (see methods).

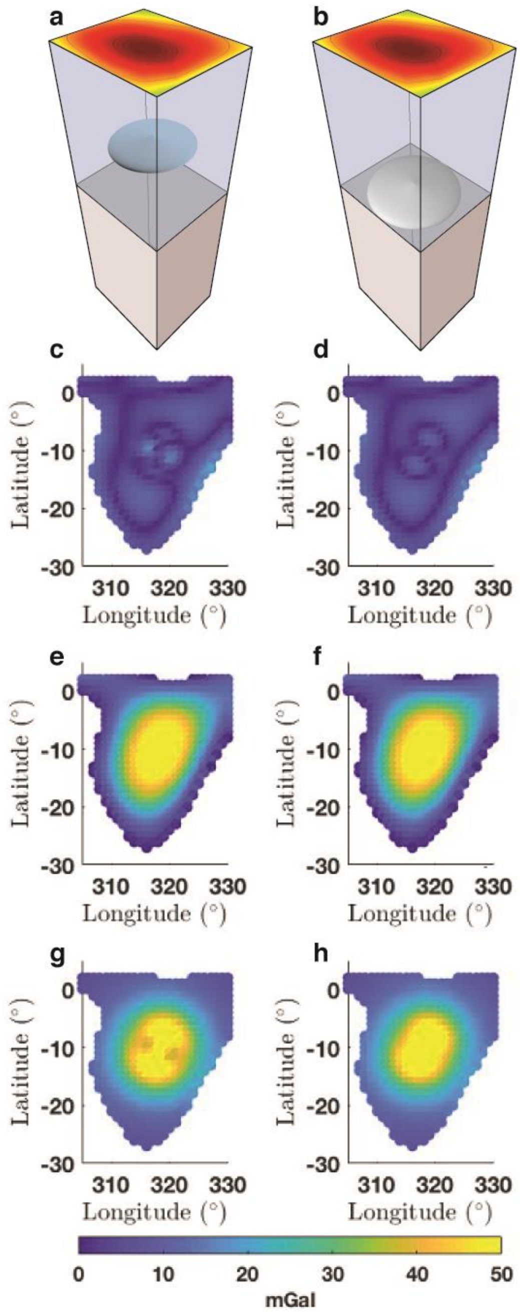

Figure 2. Gravity anomaly residuals for two solutions of the mascon analysis. a,b, Schematic representation for the two configurations with an ellipsoidal mascon located in the

crust or just above the mantle. **c,d**: Gravity anomaly residuals between Ceres18C (**e,f**), and two of the solutions of the mascon analysis (**g, h**).

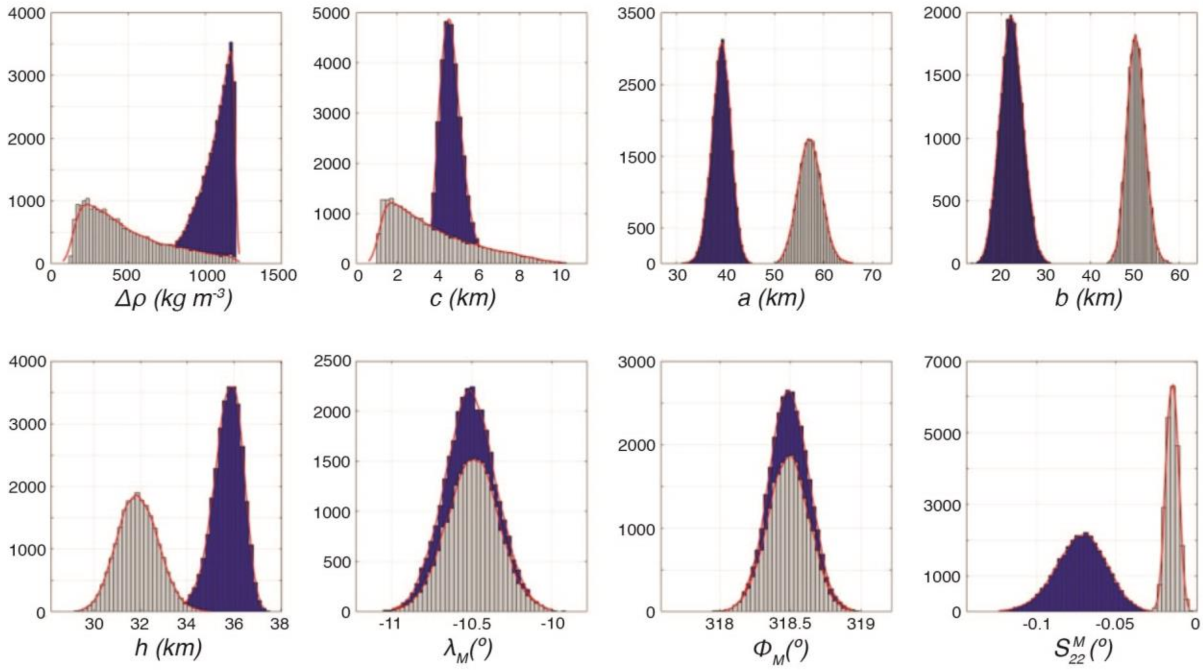

Figure 3. Mascon parameters shown as histograms of the final ensemble of solutions. The parameters are: density contrast $\Delta\rho=\rho_{mascon}-\rho_{crust}$; semi-major axes a, b, and c; depth (h) of mascon center; latitude ($\boldsymbol{\lambda_M}$); longitude ($\boldsymbol{\phi_M}$); and the gravitational parameter $\mathbf{S_{22}^M}$ that relies on its horizontal orientation. The histograms are represented by highlighting two scenarios that are consistent with the presence of a mantle uplift (blue), and filling of porosity by fluids (grey).

In the most probable scenario (~305,000 models, Figure 2b), the majority of MCMC models (70%) have a mascon density in the range of 2321-2434 kg m^{-3}, close to the mean density of the mantle. The same percentage of models have the base of the mascon within 700 m from the crust-mantle interface. The shapes of the models' ellipsoids are oblate with semi-major axes of Gaussian distributions a = 39.1 ± 2.0 km, b = 22.3 ± 2.7 km, and c = 4.7 ± 0.6 km, centered at a depth h = 35.7 ± 0.7 km. These values indicate that the mascon corresponds to mantle material found at shallower depths than expected for isostatic compensation, which we interpret as mantle uplift. Regions of positive isostatic anomaly due to mantle uplift and other processes are common on the Moon and terrestrial planets at the centers of impact craters[14], and have been suggested to explain the signature at Ceres' largest basin Kerwan[15]. An impact-triggered mantle upwelling can be excluded for that structure, however, because of the lack of large craters (>50 km) or planitie interpreted as impact basins[16] with center at Ahuna Mons. Instead, the additional mantle material may be indicative of a mantle uplift triggered by a convective plume. Whether the convection is solely the expression of hydrothermal circulation in a muddy mantle[17] or was influenced by a large basin very early in the history of Ceres[11, 16] is unclear. The feasibility of convection in the mantle of 400 km radius is tested to first order by estimating the Rayleigh number *Ra* for an ice-silicate composition with a viscosity of 10^{18} Pa s (for a mixture of ice and antigorite) and further parameters that provide a lower bound on *Ra* (see methods). Retention of interstitial fluids in the mantle[7] indicates limited warming of the body up to only few 100s K, also consistent with the mantle low density. A key implication is that uplift of the fluid-bearing mantle provides a source of fluids for the formation of Ahuna Mons. The shallowest depth of the mantle beneath the dome, and thus the depth of origin of the fluid, is represented by the top of the mascon at ~30 km.

A possible but less probable scenario of the mascon solutions (~225,000 models) shows independent Gaussian distributions of the mascon parameters compared to the previous configuration (Figure 3). In this case, the shape of the mascon is larger horizontally, and more oblate relative to the previous scenario (Figure 2a). The mascon center is deep in the crust, h = 31.8 ± 0.9 km, and is 5 km above the crust-mantle boundary. The density contrast of the mascon to the crust is less determined in this case with a peak at ρ_{mascon} = 1500-1600 kg m^{-3}. This configuration is interpreted to indicate an isolated, lenticular region within the crust of slightly higher density than the surroundings. The region might have formed by a decrease in porosity due to compaction creep of phyllosilicates if temperatures exceeded 200 K[13]. The regional decrease of the ~10 vol.% porosity[5] of the crust, however, is insufficient to create the estimated density contrast. Alternatively, the higher density could have resulted from regional filling of the void space of the crust. A likely filling material is aqueous fluids with few 10s vol.% of suspended hydrated silicate particles (~2000 kg m^{-3}) with densities close to that of the crust. The depth of the lenticular region would represent a buoyancy zone within the crust for most of the aqueous fluids. A fraction of the fluids with slightly lower density might have reached the surface and formed Ahuna Mons. In this case, the representative source point for the Ahuna Mons material is at ~28 km depth, if we assume that it corresponds to the top of the mascon. This scenario inferred from the mascon solutions provides an alternative origin depth for the fluids, although similar to the mantle uplift configuration.

Although it is not possible to distinguish between two possible configurations, we infer very similar values for the depth of origin of the fluids producing Ahuna Mons, at depth ~30 km. To assess the sensitivity of our solution to the assumed two-layer internal structure, we explored another case with a three-layer (crust, mantle, and core) internal structure. It is based on a previous study[4] that suggested the following properties for the three layers: a crustal thickness of 33 km and density of 1400 kg m^{-3}, mantle density of 2225 kg m^{-3}, and a core 200-km in size and with density 3410 kg m^{-3}. Assuming these parameters in our MCMC simulations leads to additional results (supplementary Fig. S6) that are fully in agreement with the solutions based on the two-layer interior model. Although the histograms show two separate Gaussian distributions, the final ensemble for the case based on the three-layer model offers only one scenario that is consistent with a mantle uplift. That is, both families of solutions yield a mascon located at the core-mantle boundary with a density contrast with the crust of ~800 kg m^{-3}, similar to the difference between mantle and crustal densities. The two families of solutions in the three-layer model only provide significant discrepancies in the horizontal shapes of the mascon. Thus, in the following section we are considering the MCMC configuration with the highest probability, i.e., the mantle uplift configuration with an inferred depth of fluids at ~30-km.

Slurry extrusion

We now characterize the rheology of a fluid capable of travelling through 30 km of crust while matching the high viscosity inferred from the domical landform of Ahuna Mons[9]. The factor limiting the range of fluid viscosity of a fluid ascending to form domes on Ceres is conductive cooling between the fluid and the vertical conduit wall[18]. The temperature of the wall is a function of Ceres geotherm estimated at 2.6 K/km[18], while the plausible diameter of the conduit throughout the crust is estimated at 10 m on average[18]. The initial fluid temperature is set as the minimum eutectic point for pure water (273 K). However, lower temperatures may also be possible if the liquid is a brine, i.e., an aqueous solution with dissolved salts[19]. We use an analytical solution for the conductive cooling[22] to find the minimum velocity that prevents complete freezing of the fluid during ascent to the surface. If complete freezing is achieved, then the fluid behaves as a solid and it is assumed that the flow stops within the crust. With the depth constraint of 30 km, we determined that the ascent velocity must be $>10^{-5}$ m s^{-1}. If the fluid is approximated as a Newtonian flow, then the velocity is reached with an initial viscosity lower than 10^{8} Pa s. We note that these are limit values and the fluid can have higher velocities that imply lower viscosities. Pure water or brines have sufficiently low viscosity to ascend (~10^{-2} Pa s), but at extrusion on the surface, they exhibit subtle morphologies[20] that are not observed with the Dawn observations, whose spatial resolution is sufficient to identify them[21]. The stiff morphology and high relief of the dome, instead, set a minimum viscosity of at least ~10^3 Pa s during extrusion by analogy with natural and laboratory extrusive constructs[22, 23]. The only plausible material satisfying this constraint is a fluid entrained with ~30-45 vol.% of non-soluble, solid particles, in essence a slurry (Figure 4).

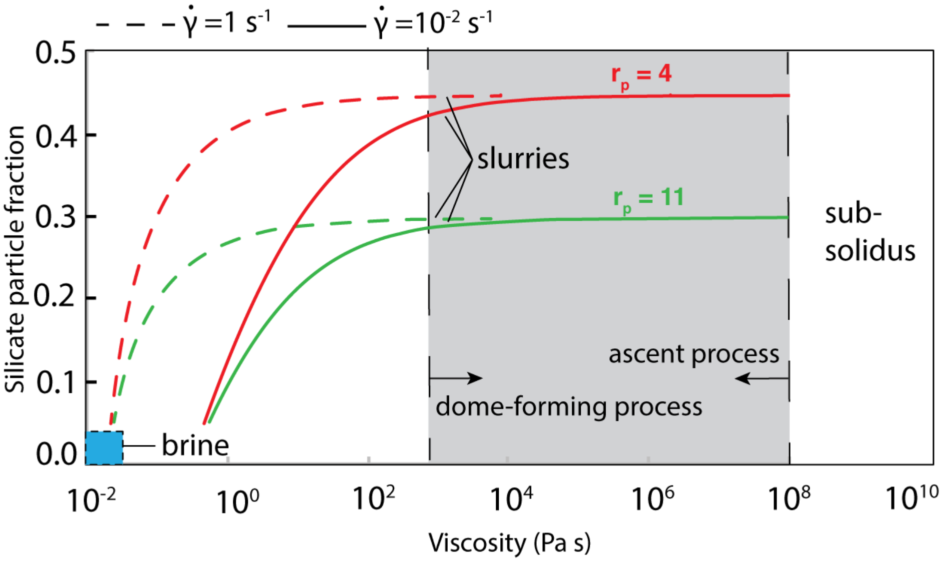

Figure 4. Constraints on the fluid properties. The solid curves represent the effects of suspended particles on the fluid rheology for particles of aspect ratio (length-to-thickness) r_p[30] For particle fraction higher than ~ 0.3, the fluids exhibit shear-thinning, and the effect of relatively high shear rate γ on the apparent viscosity is represented by the dashed curves[31]. The grey area is defined by the constraints on the lowermost viscosity from the dome surface emplacement process and the uppermost viscosity from the ascent process. For the required viscosities, a relatively high particle fraction is required. A pure brine fluid (blue inset) and a material at sub-solidus do not satisfy the constraints.

Colloidal dispersion can exhibit a non-Newtonian behaviour with low apparent viscosity at the relatively high shear rates (~1 s^{-1}) plausibly experienced during ascent. The slow growth of the dome, instead, occurred in a low shear rates regime (<10^{-2} s^{-1}), in which case the slurry behaviour is characterized by a viscosity several orders of magnitude higher than at high shear rates and produce morphologies consistent with observations[9]. The transport of non-soluble particles from depth would occur by suspension at the inferred range of ascent velocity and at the low gravity of Ceres[24].

A slurry material provides a reasonable explanation for two independent characteristics of Ahuna Mons. Whereas the spectral detection of carbonates on the dome’s walls is explained by crystallization of a salt-rich fluid[10], the co-occurrence of the spectral signature of phyllosilicates can correspond to hydrated particles of the parent slurry. From modelling of the viscous relaxation of the dome a composition of ~40 vol.% non-ice particles mixed with ice was inferred[25], a petrology that can be explained by extrusion and freezing of the proposed slurry. Extrusions of colloidal dispersions have possibly been widespread given the number of domes observed globally[26], suggesting that at least a fraction of the minerals detected at the surfaces are of endogenous origin from the deep interior, with a possible contribution from implant from impacts[27]. Our results support the scenario of a convecting, mud-bearing mantle with efficient heat dissipation, moderate heating and minor temperature variation[17,28] both for the early and, given the geologically recent emplacement of Ahuna Mons[26], likely current state of Ceres. The properties of Ceres' extrusive material differs from the solid particle-free cryovolcanic fluid[29] inferred on icy satellites, and reveals how terrestrial planets, protoplanets and icy moons display extrusive phenomena in a variety of compositional and rheological properties.

References:

1. Russell C. T. et al. Dawn arrives at Ceres: Exploration of a small, volatile-rich world. Science 353 (6303), 1008-1010 (2016).

2. Castillo-Rogez, J. C., & McCord, T. B. Ceres' evolution and present state constrained by shape data. Icarus, 205(2), 443-459. doi:10.1016/j.icarus.2009.04.008 (2010).

3. Park, R. S., et al. A partially differentiated interior for (1) Ceres deduced from its gravity field and shape. Nature, 537(7621), 515. doi:10.1038/nature18955 (2016).

4. Konopliv, A. S., et al. The Ceres gravity field, spin pole, rotation period and orbit from the Dawn radiometric tracking and optical data. Icarus, 299, 411-429. doi:10.1016/j.icarus.2017.08.005. (2017).

5. Ermakov, A. I., Fu, R. R., Castillo-Rogez, J. C., Raymond, C. A., Park, R. S., Preusker, F., et al. Constraints on Ceres' internal structure and evolution from its shape and gravity measured by the Dawn spacecraft. J. Geophys. Res, 122(11), 2267-2293. doi:10.1002/2017JE005302 (2017).

6. Mao, X. and W.B. McKinnon, Faster paleospin and deep-seated uncompensated mass as possible explanations for Ceres' present-day shape and gravity, Icarus, doi:10.1016/j.icarus.2017.08.033 (2017).

7. Fu, R. R., et al. The interior structure of Ceres as revealed by surface topography. Earth and Planetary Science Letters, 476, 153-164. doi:10.1016/j.epsl.2017.07.053 (2017).

8. Preusker, F. et al. Shape model, reference system definition, and cartographic mapping standards for comet 67P/Churyumov-Gerasimenko – Stereo-photogrammetric analysis of Rosetta/OSIRIS image data, A&A 583, A33, doi: 10.1051/0004-6361/201526349 (2015).

9. Ruesch, O., et al. Cryovolcanism on Ceres, Science 353 (6303), doi:10.1126/science.aaf4286 (2016).

10. Zambon, F., et al. Spectral analysis of Ahuna Mons from Dawn mission's visible-infrared spectrometer. Geophys. Res. Lett. 44(1), 97-104. doi:10.1002/2016GL071303 (2017).

11. Tricarico, P., True polar wander of Ceres due to heterogeneous crustal density, Nature Geoscience, doi: 10.1038/s41561-018-0232-3, (2018).

12. Formisano, M., Federico, C., De Andelis, S., De Sanctis, M. C., Magni, G. The stability of the crust of the dwarf planet Ceres, MNRAS 463, 520–528 (2016).

13. Neumann, W., Breuer, D., Spohn, T. Modelling the internal structure of Ceres: Coupling of accretion with compaction by creep and implications for the water-rock differentiation, A&A 584, doi: 10.1051/0004-6361/201527083 (2015).

14. Melosh, H. J. et al. The origin of lunar mascon basins, Science 340 (6140), 1552-1555, doi: 10.1126/science.1235768 (2013).

15. Bland, M. T. et al. Morphological indicators of a mascon beneath Ceres' largest crater, Kerwan, Geophys. Res. Lett. 45, 1297–1304. https://doi.org/10.1002/2017GL075526 (2018).

16. Marchi, S. et al. The missing large impact craters on Ceres. Nat. Commun. 7:12257 doi: 10.1038/ncomms12257 (2016).

17. Travis, B. J., et al., Hydrothermal dynamics in CM-based model of Ceres, Met. Plan. Sci., 1-25, doi:10.1111.maps.13138, (2018).

18. Quick, L. C. et al. A possible brine reservoir beneath Occator crater: thermal and compositional evolution and the formation of the Vinalia Faculae. Icarus, in press, doi:10.1016/j.icarus.2018.07.016, (2018).

19. Davis, D. W., Lowenstein, T. K., Spencer, R. J., Melting behavior of fluid inclusions in laboratory-grown halite crystals in the systems NaCl–H2O, NaCl–KCl–H2O, NaCl–MgCl2–H2O, and NaCl–CaCl2–H2O. Geo. Cosm. Acta 54, 596–601, (1990).

20. Fagents, S. A., Considerations for effusive cryovolcanism on Europa, the post-Galileo perspective, J Geophys. Res. doi:10.1029/2003JE002128, (2003)24.

21. Ruesch, O., Quick, L. C., Landis, M. E., Sori, M. M., Cadek, O., et al., Bright carbonate surfaces on Ceres as remnants of salt-rich water fountains, Icarus, in press, doi:10.1016/j.icarus.2018.01.022, (2018).

22. Blake, S. Viscoplastic models of lava domes. In J. H. Fink (Ed.), Lava flows and domes, Springer Verlag Berlin Heidelberg, (1990).

23. Spera, F. J. Physical properties of magma. In Sigurdson, H. (Ed.), Encyclopedia of volcanoes, Academic Press, New York, (2000).

24. Shields, A. Application of similarity principles and turbulence research to bed-load movement, Tech. Rep., Mitteilungen der Preussischen Versuchsanstalt fur Wasserbau und Schiffbau, Berlin (1936).

25. Sori, M. M., S. Byrne, M. T. Bland, A. M. Bramson, et al. The vanishing cryovolcanoes of Ceres, Geophys. Res. Lett., 44, doi:10.1002/2016GL072319 (2017).

26. Sori, M. M. Sizemore, H. G., Byrne, S., Bramson, A. M., Bland, M. T., Cryovolcanic rates on Ceres revealed by topography, Nature Astronomy, doi:10.1038/s41550-018-0574-1, (2018).

27. Marchi, S., et al., Manuscript under review in Nature Astronomy.

28. Neveu, M., & S. J. Desch, Geochemistry, thermal evolution, and cryovolcanism on Ceres with a muddy ice mantle, Geophys. Res. Lett., 42, 10,197–10,206, doi:10.1002/2015GL066375 (2015).

29. Kargel, J. S., Cryovolcanism on the icy satellites, Earth, Moon and Planets 67, 101-113, (1995).

30. Krieger, I. M. and T. J. Dougherty, A mechanism for non-newtonian flow in suspensions of rigid spheres, Transactions of the society of rheology 111, 137-152, (1959).

31. Sisko, A. W., The flow of lubricating greases, Ind. Eng. Chem., 50 (12) 1789-792, (1958).

Methods

1. Bouguer and Isostatic Gravity Anomalies

Dawn's radio science investigation at Ceres enabled the determination of the dwarf planet's gravity field in spherical harmonics to degree (l) and order (m) 18 [3]. This solution, named Ceres18C, is characterized by a spatial resolution of ~82 km (degree 18) at the equator and of ~105 km (degree 14) at the poles. However, the knowledge of the spherical harmonic degrees l>16 is hampered by the *a priori* constraint that was assumed in the spherical harmonic framework to estimate Ceres18C [3]. The lower degrees l<5, on the other hand, are dominated by the hydrostatic contribution of the zonal harmonics J_2 and J_4. Therefore, the range of the spherical harmonic degrees used in this study to yield gravity anomaly maps is l=5-16. This approach permits isolation of the gravity signal that is directly related to subsurface mass anomalies in the area surrounding Ahuna Mons.

A map of the free-air (FA) gravity anomalies ($\boldsymbol{g^{FA}}$) are shown in the Supplementary Fig. S1-A. A strong FA anomaly of ~100 mGal is located in the vicinity of Ahuna Mons. This strong signal accounts for the gravitational contribution of the topography and of the crust-mantle boundary variations associated with isostatic compensation. By subtracting the gravity anomalies predicted by surface topography from the FA gravity, we determined the Bouguer anomaly map (Supplementary Fig. S1-B). The assumed crustal density, ρ_c = 1287 kg m^{-3}, to compute the gravitational effect of the topography is consistent with the two-layer model by [5].

The comparison between gravity and topography, or, especially, between the measured gravity and gravity expected from topography ($\boldsymbol{g^T}$), allows us to retrieve the gravitational signal associated with relief at the crust-mantle boundary. The admittance ($\widetilde{\boldsymbol{Z}}$) represents a useful tool to provide spectral characterization of gravity and topographic data. If we adopt the gravity derived from topography, we can compute the average admittance per harmonic degree *l* as follows:

$$\widetilde{\boldsymbol{Z}}_{\boldsymbol{l}} = \frac{\boldsymbol{S}_{\boldsymbol{l}}^{\boldsymbol{g}\boldsymbol{g}^{\boldsymbol{T}}}}{\boldsymbol{S}_{\boldsymbol{l}}^{\boldsymbol{g}^{\boldsymbol{t}}\boldsymbol{g}^{\boldsymbol{T}}}}$$

where the power spectral density (PSD) $\boldsymbol{S}_{\boldsymbol{l}}^{\boldsymbol{g}\boldsymbol{g}^{\boldsymbol{T}}}$ and $\boldsymbol{S}_{\boldsymbol{l}}^{\boldsymbol{g}^{\boldsymbol{T}}\boldsymbol{g}^{\boldsymbol{T}}}$ are given by:

$$\begin{aligned} \boldsymbol{S}_{\boldsymbol{l}}^{\boldsymbol{g}\boldsymbol{g}^{\boldsymbol{T}}} &= \frac{\sum_{m=0}^{l}\left(\bar{C}_{lm}\bar{C}_{lm}^{T}+\bar{S}_{lm}\bar{S}_{lm}^{T}\right)}{2l+1} \\ \boldsymbol{S}_{\boldsymbol{l}}^{\boldsymbol{g}^{\boldsymbol{T}}\boldsymbol{g}^{\boldsymbol{T}}} &= \frac{\sum_{m=0}^{l}\left({\bar{C}_{lm}^{T}}^{2}+{\bar{S}_{lm}^{T}}^{2}\right)}{2l+1} \end{aligned} \quad .$$

These expressions rely on the spherical harmonic coefficients of the gravity field Ceres18C ($\bar{\boldsymbol{C}}_{\boldsymbol{lm}}$ and $\bar{\boldsymbol{S}}_{\boldsymbol{lm}}$) and the gravity derived from topography ($\bar{\boldsymbol{C}}_{\boldsymbol{lm}}^{\boldsymbol{T}}$ and $\bar{\boldsymbol{S}}_{\boldsymbol{lm}}^{\boldsymbol{T}}$), which is based on Dawn's High Altitude Mapping Orbit (HAMO) Stereophotogrammetry (SPG) shape model [32].

We then computed the isostatic anomalies ($\boldsymbol{g}_{\boldsymbol{l}}^{\boldsymbol{I}}$) as the difference between the measured gravity and gravity derived from topography, which is opportunely corrected for the average admittance per harmonic degree, as follows:

$$\boldsymbol{g}_{\boldsymbol{l}}^{\boldsymbol{I}} = \boldsymbol{g}_{\boldsymbol{l}}^{\boldsymbol{FA}} - \widetilde{\boldsymbol{Z}}_{\boldsymbol{l}}\boldsymbol{g}_{\boldsymbol{l}}^{\boldsymbol{T}} \quad .$$

The isostatic gravity anomaly map projected on an 482.0 × 445.9 km ellipsoid is shown in the Supplementary Fig. S2. The region surrounding Ahuna Mons has a large isostatic anomaly of ~50-60 mGal. This residual gravity signature provides crucial information on the properties of possible subsurface structures beneath the area that encompasses the cryovolcanic dome.

2. 3-D Ellipsoidal Mascon and its Gravitational effect

The gravity measurements of Ceres were previously used to determine the interior structure of the dwarf planet by assuming a global Airy isostatic compensation mechanism [5]. The isostatic gravity anomaly map shows that only few regions are characterized by substantial residual gravity that is indicative of local deviation from isostatic compensation. The departure from this state of gravitational equilibrium allows us to study the physical properties of subsurface structures.

A 3-D ellipsoidal mascon with uniform density was used to reproduce the gravity signal (Supplementary Fig. S1-B) in the vicinity of Ahuna Mons at 0-20˚S and 35-55˚W. Supplementary Fig. S2 shows the following properties of the mascon: horizontal (*a*,*b*) and vertical (*c*) axes, that correspond to the width and height of the mascon, respectively; density contrast between mascon and crustal densities ($\Delta\rho=\rho_M- \rho_c$); depth (*h*) or distance from the surface; colatitude (ϑ_M) and longitude (ϕ_M) of the mascon center; horizontal tilt angle (parameterized as the spherical harmonic coefficient $\boldsymbol{S}_{\boldsymbol{22}}^{\boldsymbol{M}}$ of the gravitational potential of the mascon). These parameters were adjusted in our study to reproduce the observed isostatic gravity anomaly. Preliminary transformation and rotation were required to compute precisely the gravitational acceleration at a generic point *P*. The isostatic gravity anomalies were retrieved on a sphere with a radius equal to Ceres' mean radius, R = 470 km. The point P is defined in the planetocentric reference frame (X,Y,Z) with spherical coordinates as $P(R, \vartheta, \phi)$, where ϕ is the longitude (305-335˚) and ϑ is the colatitude (90-110˚).

To compute the gravitational potential energy of the mascon, we projected these spherical coordinates in a reference frame with its origin at the center of the mascon (Supplementary Fig. S3). Therefore, we computed:

$$X_P - X_M = \begin{bmatrix} R\cos\phi\sin\vartheta - (R-h)\cos\phi_M\sin\vartheta_M \\ R\sin\phi\sin\vartheta - (R-h)\sin\phi_M\sin\vartheta_M \\ R\cos\vartheta - (R-h)\cos\vartheta_M \end{bmatrix}$$

where R is the mean radius of Ceres, h is the depth of the mascon, and ϕ, ϕ_M, ϑ, and ϑ_M are longitudes and colatitudes of P and the center of the mascon in the planetocentric reference frame, respectively. The resulting vector was, then, reported in the reference frame oriented with the principal axes of the mascon (x_M, y_M, z_M), as follows:

$$x_P = \begin{bmatrix} x \\ y \\ z \end{bmatrix} = R_2(\vartheta_M)R_3(\phi_M)(X_P - X_M)$$

where the rotation matrices $R_2(\vartheta_M)$ and $R_3(\phi_M)$ are defined as:

$$R_3(\phi_M) = \begin{bmatrix} \cos\phi_M & \sin\phi_M & 0 \\ -\sin\phi_M & \cos\phi_M & 0 \\ 0 & 0 & 1 \end{bmatrix} \quad R_2(\vartheta_M) = \begin{bmatrix} \cos\vartheta_M & 0 & -\sin\vartheta_M \\ 0 & 1 & 0 \\ \sin\vartheta_M & 0 & \cos\vartheta_M \end{bmatrix}.$$

Thus, the gravitational potential energy associated with the density contrast between the mascon and the crust is given by:

$$U_M = -\frac{GM_M}{r}\left[1 + \left(\frac{R_M}{r}\right)^2 C_{20}^M P_{20}(\cos\vartheta) + \left(\frac{R_M}{r}\right)^2 C_{22}^M P_{22}(\cos\vartheta)\cos 2\phi + \left(\frac{R_M}{r}\right)^2 S_{22}^M P_{22}(\cos\vartheta)\sin 2\phi\right], \qquad \text{(S7)}$$

where R_M is the mean radius of the mascon, which is assumed to be the mean equatorial radius $\left(R_M = \frac{(a+b)}{2}\right)$, $r = \sqrt{x^2 + y^2 + z^2}$ is the distance between P and the mascon center, $M_M = \frac{4}{3}\pi\Delta\rho abc$ is the incremental mass of the mascon, the unnormalized spherical harmonic coefficients C_{20}^M, and C_{22}^M relies on the size and shape of the mascon as follows:

$$C_{20}^M = \frac{1}{5R^2}\left[\left(c^2 - a^2\right) + \frac{1}{2}\left(a^2 - b^2\right)\right]$$
$$C_{22}^M = \frac{1}{20R^2}\left[\left(a^2 - b^2\right)\right]$$

and S_{22}^M describes the horizontal tilt angle of the semi-major axes a, and b. The associated Legendre and longitudinal functions depend on the relative position of P on the surface, as follows:

$$P_{20}(\cos\vartheta) = \frac{1}{2}\left[3\cos^2\vartheta - 1\right] = \frac{1}{2}\left[\frac{2z^2 - x^2 - y^2}{r}\right]$$
$$P_{22}(\cos\vartheta) = 3\left(1 - \cos^2\vartheta\right) = \frac{3\left(x^2 - y^2\right)}{r}$$

$$\sin 2\phi = \left[\frac{2xy}{x^2 + y^2}\right]$$
$$\cos 2\phi = \left[\frac{x^2 - y^2}{x^2 + y^2}\right]$$

The vertical and horizontal geometry between a generic point P and the mascon are shown in the Supplementary Fig. S4. We also discretized the mascon gravitational potential energy, U_M, by using four terms ($\boldsymbol{U_M = [U_{M1} + U_{M2} + U_{M3} + U_{M4}]}$). The first term is related to the monopole and is given by:

$$U_{M1} = -\frac{GM_M}{r}$$

and the other three represent the quadrupole terms:

$$U_{M2} = -\frac{GM_M}{r^5}\left[\left(c^2 - a^2\right) + \frac{1}{2}\left(a^2 - b^2\right)\right]\frac{\left(2z^2 - x^2 - y^2\right)}{10}$$
$$U_{M3} = -\frac{3}{20}\frac{GM_M}{r^5}\left(a^2 - b^2\right)\left(x^2 - y^2\right)$$
$$U_{M4} = -\frac{GM_M}{r^5}6xyR_M^2S_{22}^M$$

The resulting gravity anomaly ($|\boldsymbol{a_M}|$) is computed with the gradient in gravitational potential, as follows:

$$a_M = -\nabla U_M$$

The partial derivatives that are needed to determine the total gravity acceleration are given by:

$$\frac{\partial U_{M1}}{\partial x} = \frac{GM_M}{r^3}x$$
$$\frac{\partial U_{M1}}{\partial y} = \frac{GM_M}{r^3}y$$
$$\frac{\partial U_{M1}}{\partial z} = \frac{GM_M}{r^3}z$$

$$\frac{\partial U_{M2}}{\partial x} = \frac{GM_M}{r^7}x\left[\left(c^2 - a^2\right) + \frac{1}{2}\left(a^2 - b^2\right)\right]\left[\frac{\left(2z^2 - x^2 - y^2\right)}{2} + \frac{2}{5}r^2\right]$$
$$\frac{\partial U_{M2}}{\partial y} = \frac{GM_M}{r^7}y\left[\left(c^2 - a^2\right) + \frac{1}{2}\left(a^2 - b^2\right)\right]\left[\frac{\left(2z^2 - x^2 - y^2\right)}{2} + \frac{2}{5}r^2\right]$$
$$\frac{\partial U_{M2}}{\partial z} = \frac{GM_M}{r^7}z\left[\left(c^2 - a^2\right) + \frac{1}{2}\left(a^2 - b^2\right)\right]\left[\frac{\left(2z^2 - x^2 - y^2\right)}{2} - \frac{4}{5}r^2\right]$$

$$\frac{\partial U_{M3}}{\partial x} = \frac{3}{5}\frac{GM_M}{r^7}\left(a^2 - b^2\right)x\left[\frac{5}{4}\left(x^2 - y^2\right) - \frac{r^2}{2}\right]$$
$$\frac{\partial U_{M3}}{\partial y} = \frac{3}{5}\frac{GM_M}{r^7}\left(a^2 - b^2\right)y\left[\frac{5}{4}\left(x^2 - y^2\right) + \frac{r^2}{2}\right]$$
$$\frac{\partial U_{M3}}{\partial z} = \frac{3}{4}\frac{GM_M}{r^7}z\left(a^2 - b^2\right)\left(x^2 - y^2\right)$$

$$\frac{\partial U_{M4}}{\partial x} = 6\frac{GM_M}{r^7}R_M^2S_{22}^M\left[5x^2y - yr^2\right]$$
$$\frac{\partial U_{M4}}{\partial y} = 6\frac{GM_M}{r^7}R_M^2S_{22}^M\left[5xy^2 - xr^2\right]$$
$$\frac{\partial U_{M4}}{\partial z} = 30\frac{GM_M}{r^7}R_M^2S_{22}^Mxyz$$

The resulting gravity anomaly computed at a generic location *P(x,y,z)* is given by:

$$|\boldsymbol{a}^{com}| = \sqrt{\left(\frac{\partial U_{M1}}{\partial x}+\frac{\partial U_{M2}}{\partial x}+\frac{\partial U_{M3}}{\partial x}+\frac{\partial U_{M4}}{\partial x}\right)^2+\left(\frac{\partial U_{M1}}{\partial y}+\frac{\partial U_{M2}}{\partial y}+\frac{\partial U_{M3}}{\partial y}+\frac{\partial U_{M4}}{\partial y}\right)^2+\left(\frac{\partial U_{M1}}{\partial z}+\frac{\partial U_{M2}}{\partial z}+\frac{\partial U_{M3}}{\partial z}+\frac{\partial U_{M4}}{\partial z}\right)^2}$$

3. Markov-Chain Monte Carlo algorithm

The parameters of the mascon that directly affect the computation of the gravity anomalies are: the three semi-major axes *a*, *b*, and *c*; longitude ($\boldsymbol{\phi_M}$), colatitude ($\boldsymbol{\vartheta_M}$), and depth (*h*) of its center; the horizontal orientation ($\boldsymbol{S_{22}^M}$); and the density contrast with the crust ($\Delta\rho=\rho_{mascon}-\rho_{crust}$). To sample the multi-dimensional parameter space, we use the Bayesian inversion approach that is based on a Markov-Chain Monte Carlo (MCMC) algorithm [33]. The criterion that is applied to determine the resulting ensemble of models is the minimization of the differences between the local gravity map observed with Ceres18C and computed with the 3-D ellipsoidal mascon. We discretized the local map in 1-degree per pixel (dpp), and we computed the gravity anomalies in each point for both Ceres18C (only with spherical harmonic degrees $5 \le l \le 16$) and the modeled mascon. The discrepancies between computed and observed gravity anomalies are assumed to have a Gaussian distribution, and therefore, the probability function P(*j*) at each step *j* used in our algorithm is defined as follows:

$$\boldsymbol{P(j)} = \exp\left(\frac{1}{2}\left[\left(\boldsymbol{a_1^{com}}-\boldsymbol{a_1^{obs}}\right) \quad \cdots \quad \left(\boldsymbol{a_n^{com}}-\boldsymbol{a_n^{obs}}\right)\right] \times \begin{bmatrix} 1/\sigma_g^2 & \dots & 0 \\ \vdots & \ddots & \vdots \\ 0 & \cdots & 1/\sigma_g^2 \end{bmatrix} \times \begin{bmatrix} \left(\boldsymbol{a_1^{com}}-\boldsymbol{a_1^{obs}}\right) \\ \vdots \\ \left(\boldsymbol{a_n^{com}}-\boldsymbol{a_n^{obs}}\right) \end{bmatrix}\right)$$

where $\boldsymbol{a_i^{com}}$ and $\boldsymbol{a_i^{obs}}$ are the gravity anomalies at each pixel *i* computed with the mascon modeling and Ceres18C, respectively. The corresponding standard deviation of each point is assumed to be $\boldsymbol{\sigma_g}$=10 mGal, which is the accuracy of the gravity field Ceres18C at the equatorial region of the dwarf planet [4].

The probability distribution of the mascon parameters is mapped by using random walkers that are reported in the External Table 1. The parameters are initially selected and then varied randomly with certain boundary conditions. The mascon is constrained to be entirely within the crust and $\Delta\rho$ represents the density contrast with respect to the crust. For this reason, we assumed the density of the mantle (ρ_m) as the upper limit of the density of the mascon.

We computed the gravity anomalies of the mascon at each step *j*, which is the sum of the accepted mascon parameter solution *j*-1 and a random number from a Gaussian distribution times the random walker step size per each parameter. The solution *j* is accepted when the ratio $R=P(j)/P(j-1)$ is larger than a random number generated from a uniform distribution. Otherwise, a new solution is evaluated by always perturbing the previous accepted solution *j*-1 [34,35].

A proper sampling of the mascon parameters is guaranteed by the use of multiple chains that start from different random initial conditions. The number of chains considered in this study is 40. The convergence of each chain is tested every 10,000 accepted models by computing the mean value and the root mean square (RMS) of the differences between computed and measured gravity anomalies. Once these two values did not change within 10^{-4} mGal, we assumed that the chain has converged. The number of models for each chain is ~200,000, although few of them converged with ~100,000 or

~400,000 models. These extreme cases, which correspond to three chains, were not considered in our solution. The remaining chains were opportunely mixed to determine the mascon parameters.

The solutions for each chain show an RMS of the gravity residuals of ~6 mGal, which is lower than the accuracy of the gravity field in the equatorial region. However, a certain number of initial models for each chain were excluded because of their larger RMS that was related to a "burn in" period when the solutions were still approaching the target. The mixing of the chains was carried out by selecting every *k* models from one of the chains, which is also randomly chosen. This provides a downsampling of the number of models leading to a final number of 50,000 if k=4 and the minimum number of models was 200,000.

To test the validity of our results, we also tested other approaches. The probability function that includes gravity anomaly residuals per each pixel (780 points if we consider a 1-dpp map) may overweight these measurements. For this reason, we ran some cases with a probability function with only two parameters that are the mean and the RMS of the gravity anomaly residuals. The corresponding standard deviations for the mean and the RMS were 1 mGal and 10 mGal, respectively. The results of these cases did not show notable differences with the solutions presented in this study. Furthermore, we tested different resolutions of the gravity map, in particular, with 2-dpp, and 4-dpp, in order to be closer to the actual spatial resolution of the gravity field (~11˚ on the surface), and the resulting parameters of interest were consistent with the case presented in this study with 1-ddp.

4. Gravity Anomaly Residuals

The ensemble of solutions that is converged after the MCMC chain mixing shows two possible configurations of the 3-D mascon ellipsoid. Both scenarios provide gravity anomalies that are consistent with the isostatic anomaly map of Ceres18C. The gravity anomaly residuals between Ceres18C and the gravity solution of one of the models per each scenario are shown in Figure 2. The mascon solution on the left is characterized by horizontal semi-major axes a=57.9 km and b=50 km, and a vertical height c=7 km. This mascon is 32 km deep with a density contrast $\Delta\rho$~185 kg m^{-3}. This configuration is consistent with the presence of a brine, and it is representative of the solutions that show a peak at lower density contrast in Figure 3. Models with $\Delta\rho$=150-400 kg m^{-3} corresponds to ~50% of total number of models for this scenario. The remaining half of these solutions shows larger $\Delta\rho$ and a vertical semi-major axis of the mascon c between 1 and 3 km. We also reported $\Delta\rho$ as a function of the vertical height of the mascon in the Supplementary Fig. S5. Larger values of the density contrast ($\Delta\rho$ > 400 kg m^{-3}) in this scenario show small variations of the mascon vertical height leading to a peak in Figure 3.

The other solution shown in the right panels of Figure 2 represents a 3-D mascon with semi-major axis a=36.4 km, b=19.8 km, and c=5.3 km. The depth of the mascon is closer to the crust-mantle boundary (h~35.5 km), and the density contrast is $\Delta\rho$ ~ 1070 kg m^{-3}. Since the density of this mascon (ρ_{mascon}=2355 kg m^{-3}) is quite close to the assumed density of the mantle (ρ_m=2434 kg m^{-3}) and it is placed at the base of the crust, this family of solutions provides evidence of the presence of a mantle uplift in the surrounding area of Ahuna Mons.

5. Data Availability

The data CERES18C described in [5] used in this study is available at:
https://sbn.psi.edu/archive/dawn/grav/DWNCGRS_2_v2/DATA/

6. Rayleigh number

For a sub-critical Rayleigh number, the heat in a system is transferred primarily by conduction, and for a super-critical *Ra* by convection. For a bottom-heated layer case the Rayleigh number is defined as [36]:

$$\boldsymbol{Ra = \frac{\alpha g \rho^2 c_p \Delta T_D D^3}{k\eta}}$$

with the thermal expansivity α, the acceleration due to gravity g, the density ρ, the heat capacity c_p, the temperature contrast ΔT_D across the reservoir with a thickness D that is tested for convection, the thermal conductivity k, and the viscosity η. For a uniformly and internally heated sphere with a rigid outer boundary the Rayleigh number Ra_Q is defined as:

$$\boldsymbol{Ra_Q = \frac{\alpha g \rho^3 c_p Q D^5}{k^2 \eta}}$$

with the energy production Q. We used the Dawn estimates [1] for the quantities involved and typical parameter ranges for those that are not constrained further:

- H_2O volume fraction = 10 % (a conservative value; a higher water content increases *Ra* enhancing convection at low temperatures and consistent with [7] and the mantle density composed of water and antigorite)
- thermal expansivity $\alpha = 5\cdot10^{-5}$ K^{-1}
- gravitational acceleration $g = 0.15$ m s^{-2} (at the mid-depth of the mantle, i.e. at a radius of ≈ 200 km)
- density $\rho = 2400$ kg m^{-3} (the mantle density)
- heat capacity c_p varying between 700 and 1080 J kg^{-1} K^{-1} for the temperature of 200-700 K (mass fraction weighted arithmetic mean of the H_2O and chondritic heat capacities) [37-39]
- temperature contrast $\Delta T_D = 10$ K (lower bound) [13]
- mantle thickness $D = 400$ km
- thermal conductivity k varying between 2.27 and 1.62 W m^{-1} K^{-1} for the temperature of 200-700 K (volume fraction weighted arithmetic mean of H_2O and antigorite thermal conductivities) [40-42]
- viscosity η varying between $7\cdot10^{18}$ and $1.4\cdot10^{12}$ Pa s for the temperature of 200-700 K (an average of H_2O ice/water and antigorite viscosities) [43,44].
- energy production $Q = 0.96\cdot H$ where $H = 2\cdot10^{-12}$ W kg^{-1} is the present-day energy production by the long-lived radionuclides for an ordinary chondritic initial composition. The scaling of 0.96 takes into account the assumed presence of 10 vol.% of water (i.e., 4 wt.%).

As a result, for the bottom-heated case, the Rayleigh number *Ra* varies between $1.3\cdot10^3$ and $1.3\cdot10^{10}$ in the temperature range of 200-700 K. Super-critical values of $Ra > 3\cdot10^3$ are obtained for $T \geq 230$ K. For the internally driven case, the Rayleigh number Ra_Q varies between $4.2\cdot10^4$ and $6.1\cdot10^{11}$ in the temperature range of 200-700 K. The super-critical values are in between $5.7\cdot10^3$ and $3.1\cdot10^4$ depending on the convection mode and are obtained for $T \geq 180$ K and $T \geq 210$ K, respectively.

7. Viscosity estimate and particle fraction

To investigate the rheology of a fluid with suspended solid particles (slurry), we considered the model proposed in the paper of [46] that describes a Newtonian flow and also accounts for the non-Newtonian effect of shear thinning relevant at a particle fraction φ higher than ~0.3 [47]. The apparent viscosity η at a given shear rate γ is [46]:

$$\boldsymbol{\eta = \eta_\infty + k\gamma^{n-1}},$$

where η_∞ is the apparent viscosity at infinite shear rate, taken here as the viscosity of brine 10^{-2} Pa s [48]. The value for the exponential n describes the shear thinning (pseudo-plastic) for $n<1$ and is calculated from experimental studies of [49] as a function of the particle fraction φ. The parameter k is the value of η when $\gamma=1$ and is calculated using the model presented in the paper of [50]. This latter model assumes the effect of the non-spherical shape of particles [51]:

$$\boldsymbol{k = \eta_{\varphi=0}\left(1 - \frac{\varphi}{\varphi_m}\right)^{-B\varphi_m}}$$

where $\eta_{\varphi=0}$ is the viscosity for the particle-free fluid, taken as 10^{-2} Pa s [48]. The maximum particle packing fraction is φ_m and is inversely proportional to the two-dimensional aspect ratio of the particles r_p (length to width ratio). The parameter φ_m and the Einstein coefficient B have been estimated experimentally in [52] for particle sizes in the range 25-350 µm. Despite their simplicity, these two models are expected to sufficiently approximate the rheology of the considered material. The lack of further constraints on the particles' properties prevents to consider additional effects, such as the particle size distribution (we assume one size only), their deformability and aggregation [53,54], as well as on the exact temperature of the fluid [55].

References for method

32. Preusker, F., Scholten, F., Matz, K.-D., Roatsch, T., Willner, K., Hviid, S.F., Knollenberg, J., Jorda, L., Gutierrez, P.J., Kuehrt, E., et al., Shape model, reference system definition, and cartographic mapping standards for comet 67P/Churyumov-Gerasimenko - Stereo-photogrammetric analysis of Rosetta/OSIRIS image data, Astronomy and Astrophysics, vol. 583, id.A33, (2015).

33. Mosegaard, K. and Tarantola, A., Monte Carlo sampling of solutions to inverse problems. J. Geophys. Res., 100(B7), 12431-12447, (1995).

34. Metropolis, N., Rosenbluth, A. W., Rosenbluth, M. N., Teller, A. H., & Teller, E. Equation of state calculations by fast computing machines. The journal of chemical physics, 21(6), 1087-1092, (1953).

35. Hastings, W. K., Monte Carlo sampling methods using Markov chains and their applications. Biometrika, 57(1), 97-109, (1970).

36. Schubert, G., Turcotte, D. L., Olson, P., Mantle convection in the Earth and planets, Cambridge, UK, Cambridge University Press, (2001).

37. Yomogida, K., and Matsui, T, Multiple parent bodies of ordinary chondrites, Earth and Planetary Science Letters, 68, 34-42, (1984).

38. Chase, M. W. Jr., NIST-JANAF Thermochemical Tables, Fourth Edition, Journal of Physical and Chemical Reference Data, Monograph 9, National Institute of Standards and Technology, Gaithersburg, Maryland, USA, (1998).

39. Dorsey, N. E., Properties of Ordinary Water-Substance in All Its Phases: Water-Vapor, Water, and All the Ices. Reinhold Publishing Corporation, New York, American Chemical Society Monograph, Series no. 81, (1940).

40. Ramires, M. L. V., Nieto de Castro, C. A., Nagasaka, Y., Nagashima, A., Assael, M. J., Wakeham, W. A., Standard reference data for the thermal conductivity of water, Journal of Physical and Chemical Reference Data 24:1377-1381, (1995).

41. Klinger, J., Influence of a phase transition of ice on the heat and mas balance of comets. Science 209:271-272, (1980).

42. Grindrod, P. M., Fortes, A. D., Nimmo, F., Feltham, D. L., Brodholt, J. P., Vocadlo, L., The long-term stability of a possible aqueous ammonium sulfate ocean inside Titan, Icarus 197, 137-151, (2008).

43. Shoji, D., Kurita, K., Compositional diapirism as the origin of the low-albedo terrain and vaporization at mid latitude on Ceres, J. Geophys. Res., 119, 2457-2470, (2014).

44. Hilairet, N., Reynard, B., Wang, Y., Daniel, I., Merkel, S., Nishiyama, N., Petitgirard, S., High-pressure creep of serpentine, interseismic deformation, and initiation of subduction, Science 318: 1910-1912, (2007).

45. D. W. Davis, T. K. Lowenstein, R. J. Spencer, Melting behavior of fluid inclusions in laboratory-grown halite crystals in the systems NaCl–H2O, NaCl–KCl–H2O, NaCl–MgCl2–H2O, and NaCl–CaCl2–H2O. Geo. Cosm. Acta 54, 596–601 (1990).

46. Sisko, A. W., The flow of lubricating greases, Industrial and Engineering Chemistry, 1789-1792, vol. 50, no. 12 (1958).

47. Dhodapkar, S., Jacobs, K., Hu, S., Fluid-solid transport in Ducts, in Multiphase flow handbook, ed. Crowe, C. T., CRC Press, (2006).

48. Weisbrod, N, Yechieli, Y., Shandalov, S., Lensky, N., On the viscosity of natural hyper-saline solutions and its importance: the dead sea brines, J. of. Hydrology, 532, 46-51, (2016).

49. Turian, R. M., Ma, T. W., Hsu, F. L. G., Sung, D. J., Characterization, settling, and theology of concentrated fine particulate mineral slurries, Powder Technology, 93, 219-233, (1997).

50. Krieger, I. M., and Dougherty, T. J., A mechanism for non-newtonian flow in suspensions of rigid spheres, Transactions of the society of theology, 3, 137-152, (1959).

51. Kruif, C. H., van Iersel, E. M. F., Vrij, A., Russell, W. B., Hard sphere colloidal dispersions: viscosity as a function of shear rate and volume fraction, J. Chem. Phys., 82 (9), (1985).

52. Mueller, S., Llewellin, E. W., Mader, H. M. The rheology of suspensions of solid particles, *Proc. R. Soc. A.* **466**, 1201-1228, doi: 10.1098/rspa.2009.0445 (2010).

53. Genovese, D. B., Shear rheology of hard-sphere, dispersed , and aggregated suspensions, and filler-matrix composites, Adv. Colloid. Inter. Sci., 171-171, (2012).

54. Tadros, T. F., Rheology of dispersions: principles and applications, Wiley-vch Verlag GmbH and Co., KGaA, Weinheim, (2010).

55. Darby, R., Chemical engineering fluid mechanics, Marcel Dekker, Inc., New York, (2001).